AGU ADVANCING EARTH AND SPACE SCIENCE

Geophysical Research Letters®

RESEARCH LETTER
10.1029/2022GL101842

Key Points:

- Mantle flow leads to inwardly convergent tractions around the edges of cratons, and compressive stress within
- Convergent tractions result from the downward diversion of mantle flow
- This convective self-compression could help stabilize older lithosphere against convective erosion

Supporting Information:

Supporting Information may be found in the online version of this article.

Correspondence to:

J. Paul,
jyotirmoy.paul@uni-bayreuth.de

Citation:

Paul, J., Conrad, C. P., Becker, T. W., & Ghosh, A. (2023). Convective self-compression of cratons and the stabilization of old lithosphere. *Geophysical Research Letters*, *50*, e2022GL101842. https://doi.org/10.1029/2022GL101842

Received 30 OCT 2022
Accepted 22 JAN 2023

Author Contributions:

Conceptualization: Jyotirmoy Paul, Clinton P. Conrad, Thorsten W. Becker
Formal analysis: Jyotirmoy Paul
Funding acquisition: Jyotirmoy Paul
Investigation: Jyotirmoy Paul, Clinton P. Conrad, Thorsten W. Becker, Attreyee Ghosh
Methodology: Jyotirmoy Paul, Attreyee Ghosh
Software: Jyotirmoy Paul, Thorsten W. Becker
Supervision: Clinton P. Conrad, Thorsten W. Becker, Attreyee Ghosh
Writing – original draft: Jyotirmoy Paul
Writing – review & editing: Jyotirmoy Paul, Clinton P. Conrad, Thorsten W. Becker, Attreyee Ghosh

Convective Self-Compression of Cratons and the Stabilization of Old Lithosphere

Jyotirmoy Paul[1], Clinton P. Conrad[2], Thorsten W. Becker[3,4,5], and Attreyee Ghosh[6]

[1]Bayerisches Geoinstitut, Universität Bayreuth, Bayreuth, Germany, [2]Centre for Earth Evolution and Dynamics (CEED), Department of Geosciences, University of Oslo, Oslo, Norway, [3]Jackson School of Geosciences, Institute for Geophysics, The University of Texas at Austin, Austin, TX, USA, [4]Department of Geological Sciences, Jackson School of Geosciences, The University of Texas at Austin, Austin, TX, USA, [5]Oden Institute for Computational Engineering & Sciences, The University of Texas at Austin, Austin, TX, USA, [6]Centre for Earth Sciences, Indian Institute of Science, Bangalore, India

Abstract Despite being exposed to convective stresses for much of the Earth's history, cratonic roots appear capable of resisting mantle shearing. This tectonic stability can be attributed to the neutral density and higher strength of cratons. However, the excess thickness of cratons and their higher viscosity amplify coupling to underlying mantle flow, which could be destabilizing. To investigate the stresses that a convecting mantle exerts on cratons that are both strong and thick, we developed instantaneous global spherical numerical models that incorporate present-day geoemetry of cratons within active mantle flow. Our results show that mantle flow is diverted downward beneath thick and viscous cratonic roots, giving rise to a ring of elevated and inwardly-convergent tractions along a craton's periphery. These tractions induce regional compressive stress regimes within cratonic interiors. Such compression could serve to stabilize older continental lithosphere against mantle shearing, thus adding an additional factor that promotes cratonic longevity.

Plain Language Summary Cratons are the oldest continental relicts on Earth. Due to plate tectonics and mantle convection, many non-cratonic rocks get recycled. However, cratons have escaped tectonic recycling, and some have remained stable for more than ~3 billion years. Previous studies have shown that cratons' high strength and neutral buoyancy provide them with tectonic stability. Here we show that the deep roots of cratons also help to stabilize them. This is because mantle flow is deflected downward beneath thick cratonic roots, and this deflection generates a ring of inwardly-directed forces around the edges of the craton. These inward forces compress the craton interior. Such self-induced compressive stresses may further help to stabilize Earth's oldest lithosphere.

1. Introduction

Cratons are relics of the oldest continental lithosphere, surviving since the Archean (Pearson et al., 2021). Structurally, cratons have thick lithospheric roots, or cratonic keels (Gung et al., 2003; Polet & Anderson, 1995), that are likely cold as expressed by their fast seismic velocities (Auer et al., 2014; Ritsema et al., 2011; Simmons et al., 2010). Low measured heat fluxes of cratonic lithosphere reaffirm the argument for colder cratons (Rudnick et al., 1998). The endurance of Archean cratons against Earth's tectonic and convective recycling is highly debated (cf. Yoshida & Yoshizawa, 2021), but proposed reasons for cratonic stability draw from geochemical and geophysical perspectives (Jordan, 1975, 1978; King, 2005; Lenardic & Moresi, 1999; Lenardic et al., 2003; O'Neill et al., 2008; Paul & Ghosh, 2020; Paul et al., 2019; Sleep, 2003; Wang et al., 2014; Yoshida, 2012). One of the oldest hypotheses proposed that cratons are constituted of chemically lighter elements that help them to float above the convective mantle without sinking into it (Jordan, 1975, 1978). However, subsequent numerical models showed that chemical buoyancy alone cannot protect cratons from the continuous convective shearing exerted by mantle flow. Instead, root thickness and viscosity are the two prime factors that can resist deformation against mantle shearing (Lenardic & Moresi, 1999; Lenardic et al., 2003; O'Neill et al., 2008; Paul & Ghosh, 2020; Paul et al., 2019; Sleep, 2003; Yoshida, 2012).

To understand the role of craton viscosity, previous studies quantified the nature of tractions exerted by mantle flow at the base of the lithosphere, and the strain-rates associated with deformation there (Conrad & Lithgow-Bertelloni, 2006; Cooper & Conrad, 2009; Naliboff et al., 2009; Paul et al., 2019). Conrad and Lithgow-Bertelloni (2006) showed that tractions increase as lithospheric thickness increases. Paul et al. (2019)

found a similar amplification of tractions, but also showed that the strain-rates at the cratonic base diminish as lithospheric roots get thicker. This inverse relation between tractions and the strain-rates may slow the deformation of a cratonic root, and therefore might be an important factor for the long-term survival of cratons. Cooper and Conrad (2009) attributed elevated tractions at the base of cratons to greater coupling to mantle flow, which has been noted in models with thick cratonic roots (Becker, 2006; Zhong, 2001). However, more recent models, especially those employing free-slip surface boundary conditions that more closely resemble Earth's own conditions, show that tractions are primarily amplified along the periphery of cratons (Figure 3 from Paul et al., 2019). Although Paul et al. (2019) speculated that cratonic edges might more effectively absorb mantle stresses compared to cratonic interiors, a proper quantitative analysis of such a phenomenon is lacking.

Here, we explore the origin of higher tractions along craton boundaries and consider their implications for the stability of cratons. We build instantaneous global models of mantle convection and examine how mantle flow is modified due to the presence of thick and viscous cratons. We hypothesize that the diversion of mantle flow by the thick and highly viscous root of a craton can generate strong and inwardly-convergent tractions at the craton's periphery. We test our hypothesis using various models with different viscosity combinations for cratons and asthenosphere. We consider how large convergent tractions, which are generated by the cratons themselves, may support cratonic stability against mantle shearing, and therefore could be essential for cratonic longevity.

2. Mantle Convection Models

We use the finite element code CitcomS to develop instantaneous spherical models of mantle convection (Zhong et al., 2000). The code assumes the mantle to be a viscous and incompressible fluid. It solves the conservation of mass, momentum, and energy equations with the Boussinesq approximation and infinite Prandtl number. The smallest resolution of our models in the horizontal direction is ~0.7° × 0.7°. The vertical resolution in the top 300 km is 24 km, and from 300 km to the core-mantle boundary (CMB) it is ~50 km. Mantle flow is driven by the density anomalies obtained from SMEAN2 seismic tomography (Jackson et al., 2017), which is a combination of S40RTS (Ritsema et al., 2011), GyPSuM-S (Simmons et al., 2010) and SAVANI (Auer et al., 2014). Following earlier, similar efforts (Becker, 2006; Paul & Ghosh, 2020), a velocity-density scaling value of 0.25 is used to convert velocity anomalies into density anomalies. Higher velocity regions under the continents were removed down to 300 km to impose neutrally buoyant cratons. We keep a free-slip boundary condition at the surface and at the CMB. Reference viscosity, Rayleigh number, thermal expansivity and thermal diffusivity values are kept at $\eta_{ref} = 10^{21}$ Pa.s, $Ra = 4 \times 10^8$ (considering Earth radius as the length scale), $\alpha = 3 \times 10^{-5}$ K^{-1}, and $\kappa = 10^{-6}$ m^2/s, respectively.

In our models, the mantle is divided into four layers based on their relative viscosity with respect to the upper mantle (300–600 km) reference viscosity ($\eta_{ref} = 10^{21}$ Pa.s). The top 100 km is assigned as the lithosphere with a radial viscosity of $30 \times \eta_{ref}$ (30×10^{21} Pa.s). The radial viscosity of the asthenosphere (100–300 km) is varied between 0.01 (10^{19} Pa-s), 0.1 (10^{20} Pa-s) and 1 (10^{21} Pa-s) times the reference upper mantle viscosity. The radial viscosity of the lower mantle (660–2,900 km) is made 50× larger than the reference viscosity (50×10^{21} Pa.s). On top of this radially-varying viscosity structure, we impose lateral viscosity variations. In the top 300 km, we approximate temperature-dependent viscosity using a linearized Arrhenius law $\eta = \eta_R \times \exp(E(T_0 - T))$, where η_R is the radial viscosity of any layer, T_0 is the non-dimensionalized reference temperature, and T is the non-dimensionalized actual temperature, where the maximum temperature corresponds to 1,300°C. E is a dimensionless quantity that controls the strength of the temperature dependence. We have tested several models to find suitable values for E (cf. Paul et al., 2019) and use a value of 5, which produces 10× weak plate margins compared to the continental interiors. Weak plate margins originate due to slow velocity anomalies inherent within the SMEAN2 tomography model. Stronger continental interiors with weaker plate margins enhance plateness and produce plate velocities comparable to observations (Figure S1 of Paul et al., 2019). We also incorporate high viscosity cratons in our models, where the locations of cratons are taken from the 3SMAC model (Nataf & Ricard, 1996). Cratons are made 10×, 100×, and 1,000× more viscous than the surrounding lithosphere, making their actual viscosities 30×10^{22} Pa.s, 30×10^{23} Pa.s and 30×10^{24} Pa.s, respectively. Cratons have uniformly viscous keels up to a depth of 300 km. Our reference models omit cratons and only incorporate temperature-dependent viscosity to create lateral viscosity variations.

3. Tractions Within Cratons

We analyze the $r\phi$ and $r\theta$ components of stress tensor (σ_{ij}; $i,j = r$: radial component, ϕ: longitudinal component, θ: co-latitudinal component) from model outputs and calculate traction vectors $\left(\vec{\tau}_0\right)$ from the reference model (Figure 1). In the reference model, the magnitudes of traction vectors are less than ~5 MPa, and their orientations are guided by density anomalies within the model (Figure 1a). Incorporating 100× viscous cratons in the same model significantly affects traction vectors $\left(\vec{\tau}\right)$ along the edges of cratons (Figure 1b). A few enlarged maps near the cratonic regions show this effect more prominently (Figures 1c–1i). Most cratons show rings of high traction magnitude along their periphery, where traction directions become inwardly convergent. Elevated inwardly convergent tractions appear prominently along the western margin of the North and South American cratons (Figures 1c and 1d), the eastern, western and southern margins of the Siberian and Australian cratons (Figures 1e and 1f), the northern and southern margins of the Scandinavian craton (Figure 1g), and the eastern margins of African cratons (Figure 1h). The Indian craton, being very small in size, experiences convergent tractions all around its periphery (Figure 1i). The southernmost part of the African craton shows an outwardly directed traction, which is the only exception (Figure 1h). We have tested a model with high lithospheric viscosity (150×) and similarly found large traction ratios along cratons' periphery (Figure S1 in Supporting Information S1).

To quantify the increase in traction magnitudes caused by the presence of cratons, we normalize the traction magnitudes from models with cratons using those from the reference model $\left(|\vec{\tau}|/|\vec{\tau}_0|\right)$. In the presence of cratons that are 100× more viscous than the rest of the lithosphere, the maximum traction ratio increases by up to 80–100 times at ~120 km depth along the edges of cratons (Figures 1c–1i). The magnitude of the traction ratio along the craton edges can be influenced by the viscosity structure imposed in our models (Figure 2). To investigate the dependence of the traction ratio on viscosity structure and depth, we calculate the average traction ratio at various depths along the edges of cratons (Figure 2a). The edges of cratons are identified by regions with traction ratio $\left(|\vec{\tau}|/|\vec{\tau}_0|\right)$ more than 5 at 120 km depth (Figures 1c–1i). The general trend shows that the average traction ratio varies between 10 and 15 within the top 100 km of craton edges (Figure 2a), which are proximal to viscous non-cratonic lithosphere. The average traction ratios increase with depth, reaching peak values in the mid-cratonic depth range of ~160 km. The highest traction ratio occurs near the depth of peak horizontal velocity, which occurs in the mid-asthenosphere. With increasing depth, the traction ratio gradually falls before reaching another smaller peak near the base of cratons at ~270 km depth (Figure 2a). The magnitude of the traction ratio depends on the combination of the craton and asthenosphere viscosity. Higher viscosity contrast between a craton and its surroundings can enhance traction ratio. Indeed, highly viscous (1,000×) cratons exhibit the largest traction ratios, which exhibit peak values of 35–45 for mid-asthenospheric depths. Models with smaller viscosity contrasts (e.g., stronger asthenosphere with relative viscosity 1×) exhibit relatively smaller traction ratios near the craton edges.

We use centroid moment tensor (CMT) type symbols (Figure 1) to quantify the state of stress within cratons due to inwardly convergent tractions. CMT symbols are colored by the ratio of mean horizontal stress ($\sigma_h = \frac{1}{2}(\sigma_{\phi\phi} + \sigma_{\theta\theta})$) and the second invariant of the deviatoric stress $\left(\sigma_{II} = \sqrt{\sigma_{ij}\sigma_{ij}}\right)$. A negative ratio ($\sigma_h/\sigma_{II} < 0$) indicates a compressive stress regime and vice-versa. The deformation states shown imply that the model without cratons (Figure 1a) has compression only along the convergent plate boundaries, that is, along the margins of the Pacific and the Indo-Eurasia collision zones. The same model with 100× viscous cratons (Figures 1b–1i) acquires a compressive stress regime within all cratons, except in South Africa (near the Kalahari and Kaapvaal cratons) (Figure 1h). This compressive nature is consistent throughout the cratonic root at greater depths (Figure S2 in Supporting Information S1).

4. Origin of Compression Along Craton Edges

Our models demonstrate an amplification of tractions $\left(\vec{\tau}\right)$ along craton edges that induce a highly compressive state within viscous cratons. To understand the origin of this regional compressive stress regime, we calculate the traction vector $\left(\vec{\tau}\right)$ from the $\sigma_{r\phi}$ and $\sigma_{r\theta}$ components of the deviatoric stress tensor that relate to horizontal shear,

$$\sigma_{r\phi} = 2\eta\left(\frac{\partial v_\phi}{\partial r} + \frac{\partial v_r}{\partial \phi}\right) \quad (1)$$

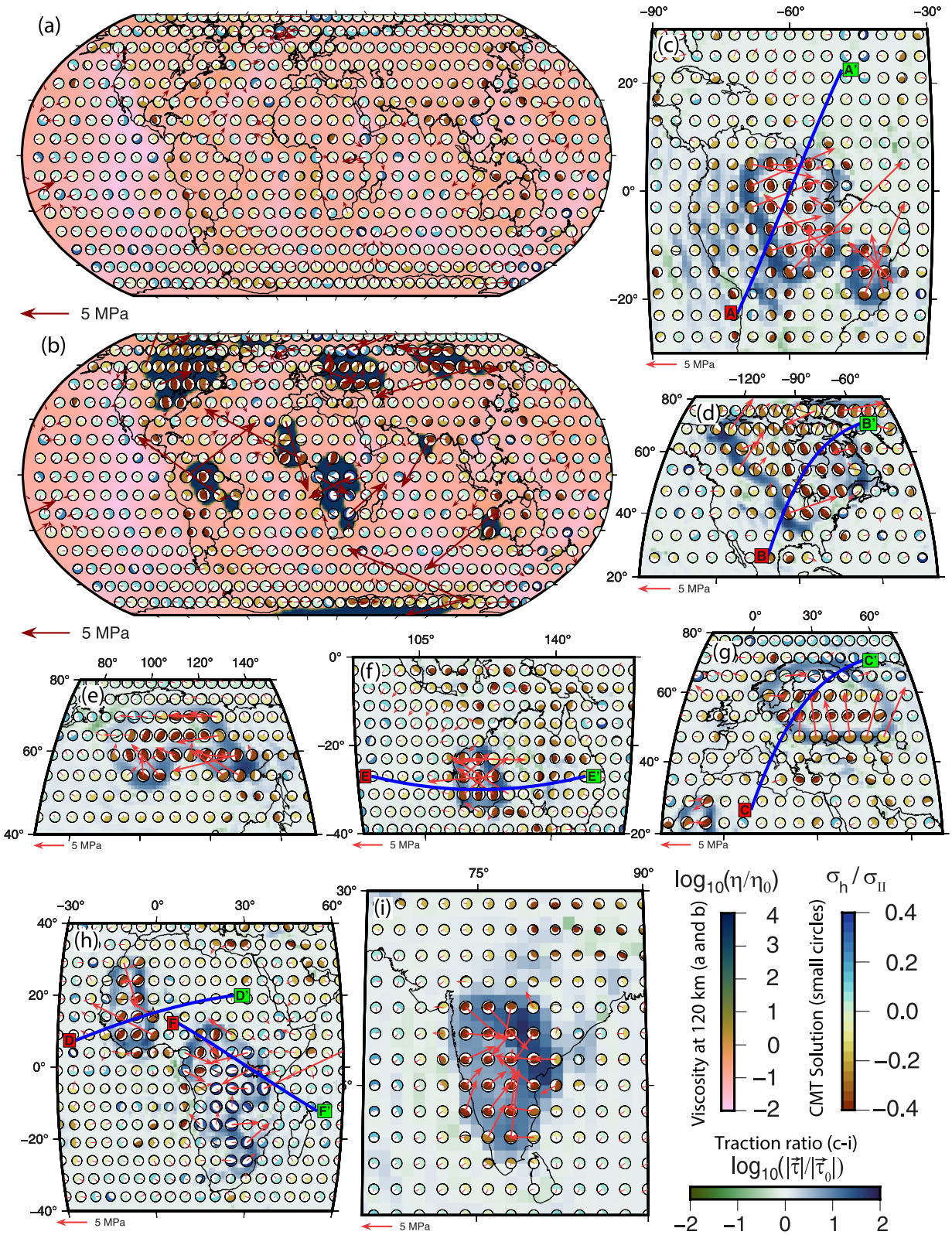

Figure 1.

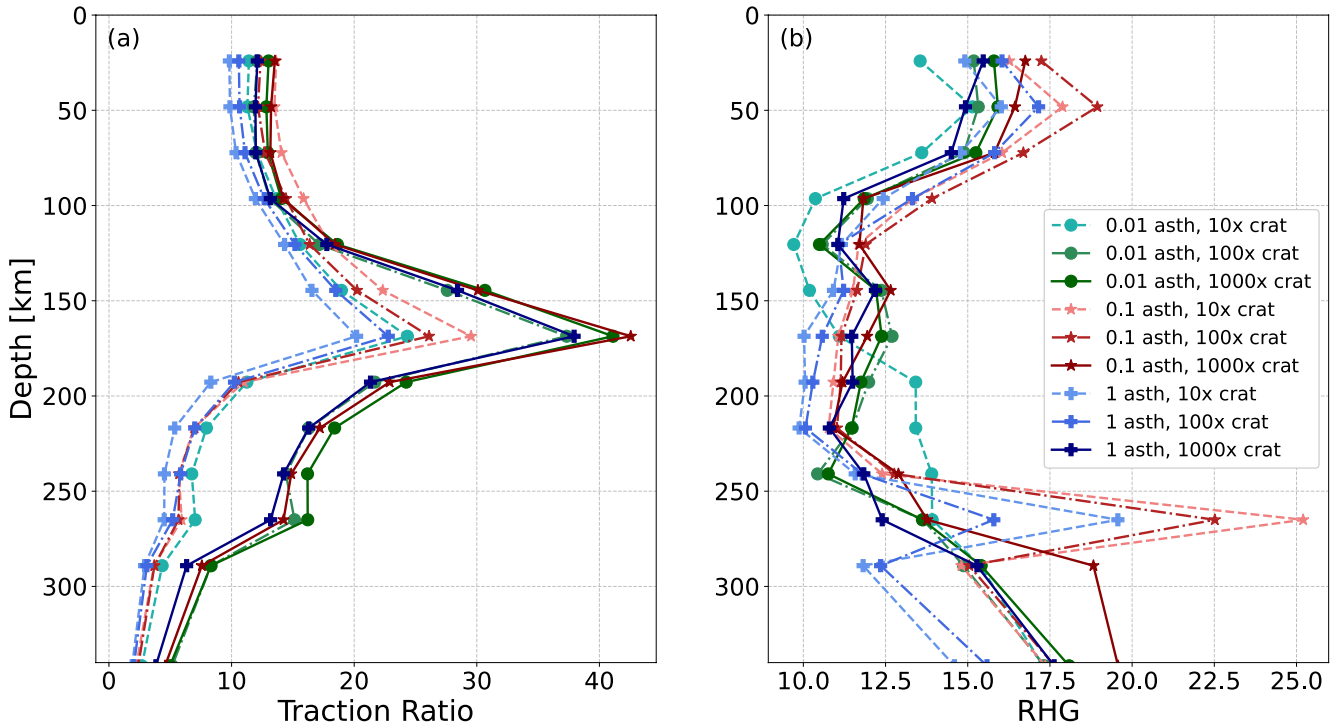

Figure 2. (a) Depth variation of the average traction ratio along the craton periphery (defined as regions where $|\vec{\tau}|/|\vec{\tau}_0| > 5$ at 120 km depth for different models. (b) Depth variation of the ratio of the horizontal velocity gradient (RHG) within regions having RHG value > 5. A description of the different models is given in the index box. The first number in the box indicates the relative viscosity of the asthenosphere, and the second number indicates the viscosity of cratons with respect to the lithosphere.

$$\sigma_{r\theta} = 2\eta\left(\frac{\partial v_\theta}{\partial r} + \frac{\partial v_r}{\partial \theta}\right) \tag{2}$$

where v_ϕ, v_θ, and v_r are the horizontal and vertical components of the velocity vector and η is the viscosity. If these shear components dominate the stress tensor, then the magnitude of horizontal traction is given by

$$|\vec{\tau}| = 2\eta\sqrt{\left(\frac{\partial v_\phi}{\partial r} + \frac{\partial v_r}{\partial \phi}\right)^2 + \left(\frac{\partial v_\theta}{\partial r} + \frac{\partial v_r}{\partial \theta}\right)^2} \tag{3}$$

The presence of a thick and highly viscous craton obstructs horizontal asthenospheric flow, and deflects it downward near the craton edges. Such velocity diversion can make the $\frac{\partial v_\phi}{\partial r}$ and $\frac{\partial v_\theta}{\partial r}$ components small near the craton edges, implying that the first terms in Equations 1 and 2 can be neglected. With stronger downward diversion, the vertical velocity (v_r) increases approaching a craton edge. Thus, the horizontal gradient of the vertical velocity component, that is, the second term in Equations 1 and 2, becomes the controlling factor for the origin of high tractions along craton boundaries. A small change in velocity gradients near cratons can thus induce higher tractions around them as tractions originate from velocity gradients multiplied by the high viscosity of cratons (Equation 3).

Large horizontal gradients of vertical velocities, induced by viscosity heterogeneity associated with cratons, thus amplify tractions. We calculate such gradients as:

Figure 1. Global traction patterns and stress regimes in the absence and presence of cratons at 120 km depth. (a) Tractions in the reference model (relative viscosity of asthenosphere is 0.1, actual asthenosphere viscosity is 10^{20} Pa.s) without cratons, (b) Tractions in a model with 0.1 relative viscosity of asthenosphere and cratons that are 100× more viscous (actual craton viscosity is 30×10^{23} Pa.s) than the surrounding lithosphere. Background colors in the global plots (a, b) indicate viscosity, and arrows represent the magnitude and direction of absolute tractions. Centroid moment tensor symbols are colored as the ratio of mean horizontal stress to the second invariant of deviatoric stress (σ_{ii}/σ_{II}), where negative values represent compressive stress regimes. (c–i) Zoomed-in plots near the cratonic regions of South America (c), North America (d), Siberia (e), Scandinavia (f), Australia (g), Africa (h), and India (i). The background colors in (c–i) represent the logarithm of the traction ratio $\left(\log_{10}\left(|\vec{\tau}|/|\vec{\tau}_0|\right)\right)$. Velocity cross-sections along the six transects (AA'–FF') are shown in Figure 4.

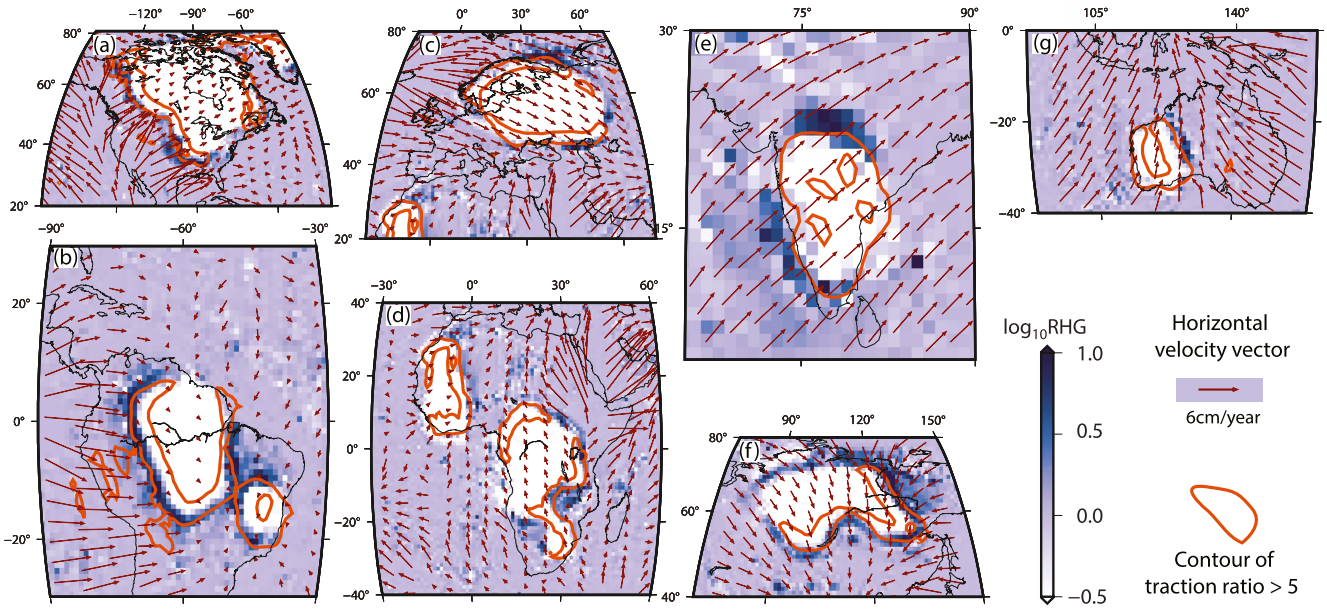

Figure 3. Zoomed-in maps of the ratio of horizontal gradients of vertical velocity (RHG) at 120 km depth near different cratonic regions from a model with 0.1 relative viscosity of asthenosphere and 100× more viscous cratons than the surrounding lithosphere. Horizontal velocity vectors at 120 km depth are plotted on top of it. Orange lines encircle areas where $|\vec{\tau}|/|\vec{\tau}_0| > 5$ at 120 km depth.

$$\nabla_h^v = \sqrt{\left(\frac{\partial v_r}{\partial \phi}\right)^2 + \left(\frac{\partial v_r}{\partial \theta}\right)^2} \tag{4}$$

To highlight the impact of thick cratons on the gradient, we compute the ratio of the horizontal velocity gradient (RHG) as:

$$\mathrm{RHG} = \frac{\left(\nabla_h^v\right)_{\mathrm{craton}}}{\left(\nabla_h^v\right)_{\mathrm{no\_craton}}} \tag{5}$$

where $\left(\nabla_h^v\right)_{\mathrm{craton}}$ and $\left(\nabla_h^v\right)_{\mathrm{no\_craton}}$ are the horizontal gradient of vertical velocities from models with and without cratons, respectively. RHG can quantify the concentration of downward flow due to the presence of viscous cratons, where RHG $\gg 1$ indicates strong vertical velocity deflection.

Similar to the rings of high traction zones, we find rings of elevated RHG along the craton periphery (Figure 3). Elevated RHG values can be interpreted as horizontal velocities converting into vertical velocities near the craton boundary due to cratons' excess thickness and viscosity. Horizontal gradients of vertical velocity should amplify tractions, and indeed contours of traction ratio >5 typically lie next to regions of high RHG values (Figure 3). The reduction of horizontal velocity at craton edges is clearly visible underneath North and South America (Figures 3a and 3b). The strong velocity decrease arises because slabs underneath these two cratons force a rapid asthenospheric flow that is impeded by stiff cratons. The velocity gradient variations expressed by RHG are also controlled by the angle between the craton edge and the direction of horizontal flow. In our density-driven flow models, the mantle flows from west to east under the North American plate, remaining almost perpendicular to the western face of the craton (Figure 3a). Hence, the maximum velocity diversion, or highest RHG value, occurs along the western margin of the North American craton. On the contrary, the southeastern margin of the craton, being almost parallel to flow, shows no significant change in RHG values. This pattern resembles the change of traction vectors along the western and eastern margins of the North American craton (Figure 1d), where elevated tractions are observed, but not on the southern and northern margins. Other cratonic edges with large RHG values include the western margins of the South American (Figure 3b) and Indian (Figure 3e) cratons, the northern and southern margins of the Scandinavian craton (Figure 3c), the eastern margins of the African cratons (Figure 3d), and the eastern and northern margins of the Siberian (Figure 3f) and Australian (Figure 3g) cratons.

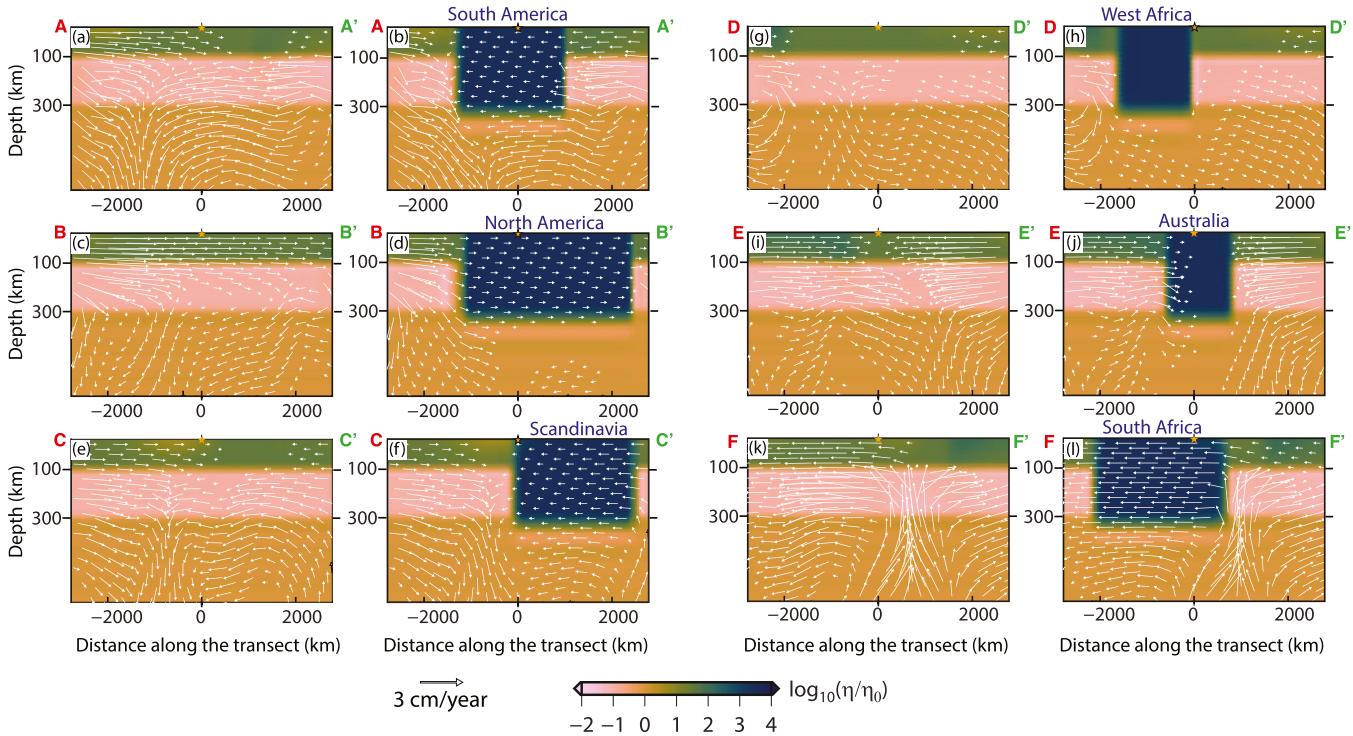

Figure 4. Comparison of velocity cross-sections up to 600 km depth with and without cratons along the transects shown in Figures 1c–1i. Each figure is paired where the left figure shows the velocity profile without a stiff craton, and the right figure shows the same with craton. The name of the continental mass that contains the craton is given for all corresponding right-side figures. Background colors represent the logarithm of relative viscosity, and the arrows represent velocity vectors along the transect.

To investigate how downwelling on the craton edges varies with depth and viscosity structure, we calculate variations of average RHG within the region where RGH value > 5 (Figure 2b). In the top 100 km, the average RHG varies within 15–17. In the mid-cratonic depth range (100–250 km), the average RHG value decreases to slightly less than 12.5. Deeper than 250 km depth, RHG increases again, reaching a peak near the base of cratons. These two peaks near the top and bottom of craton may appear due to the most significant change of velocity gradients occurring above and below the asthenosphere, giving rise to a "z" type velocity profile, considering left to right horizontal flow (e.g., Figure 4d).

We compare the velocity cross-sections from our models with and without cratons (Figure 4) to investigate the actual nature of flow diversion along craton edges. Downward mantle flow near craton edges has previously been attributed to lateral temperature variations (i.e., edge-driven convection, e.g., King and Ritsema, 2000), but our results suggest that such flow diversion is a natural consequence of global mantle convection operating in the presence of lithospheric viscosity heterogeneity. Cross-sections underneath the South American and the North American cratons show the most notable changes in velocity along their western margins (Figures 4a–4d). In both cases, the mantle flows from west to east in the absence of a craton due to density heterogeneity present in our models (Figures 4a and 4c). Convergent flow west of the South American craton occurs due to the subducting Nazca slab. In the presence of a thick and viscous craton, the convergent flow velocity is diverted along the craton margin and gets concentrated below it (Figure 4b). Similar velocity diversion is also visible around the western margin of the North American craton, where the flow gets diverted downwards and is concentrated below the craton (Figure 4d). Flow diversion by the Scandinavian craton occurs along a north-south orientation (Figures 4e and 4f). However, the diversion is relatively weaker, most likely due to the absence of nearby mantle slabs to drive the flow in the model. Weaker velocity diversion is also reflected in less elevated traction magnitudes compared to the American cratons. The size of the Western African craton is significantly smaller than the rest, but the change of velocity field is considerably pronounced (Figures 4g and 4h). A downward flow along the eastern margin of the craton denotes the change in RHG (Figure 4h). The Australian craton also shows velocity diversion (Figures 4i and 4j) along an east west profile, leading to amplified tractions. The South African craton

is different from the other cratons because of upwelling mantle flow below it (Figure 4j). In this scenario, the horizontal velocities get diminished due to the craton, and vertical upward velocities on the eastern side become stronger along the craton boundary. Therefore, the traction magnitudes increase along the South African craton's southeastern margin near the Kalahari and Kaapvaal cratons, as they do for the other cratons, but the tractions are outwardly directed and the stress regime becomes extensional (Figure 1h). Such extension could be a potential reason for recent thinning of the Kaapval craton (cf. Mather et al., 2011).

5. Role of Self-Compression in Craton Stabilization

Understanding cratonic survival has remained a long-standing problem in the geoscience community. Bedle et al. (2021) noted three significant geodynamical properties of a stable craton: (a) thick and buoyant cratonic roots, (b) highly viscous roots, and (c) integrated high yield strength that minimizes deformation. However, depending on their evolution, cratons can become unstable or partially destroyed (Bedle et al., 2021; Lee et al., 2011). For example, rapidly thickened lithosphere (e.g., Beall et al., 2018) can be subjected to basal erosion, subsequently leading to destabilization (Lenardic & Moresi, 1999). Thus, a self-driven and sustained process of gradual thickening may be essential to craton stabilization. Wang et al. (2018) has previously attributed such self-thickening to tectonic shortening stabilized by gradual gravitational thickening. However, they did not explore the nature of the stresses and tractions acting within the cratons, which may underpin slow and gradual thickening. We infer that such slow thickening could be controlled by self-compression within cratons and may be crucial for craton stabilization. Recently, a study suggested that the Slave craton may have regrown with time after being destroyed by the McKenzie plume (Liu et al., 2021). Self-compression could support such recratonization.

The shape of cratonic roots can influence the diversion of flow along the craton boundary, which subsequently deforms the craton interior (Cooper et al., 2021; Currie & van Wijk, 2016). Cooper et al. (2021) showed that a vertical craton margin can resist such deformation compared to margins that slope downward toward the craton interior. Our models consider roots with a sharp vertical viscosity contrast between the craton and the surrounding asthenosphere. In the future, it will be interesting to investigate the nature of flow diversion for cratons of different root geometries and more gradual viscosity contrasts with their surroundings. However, the horizontal length scale of the mantle flow diversion is on the order of 1,000 s of km (e.g., Figure 4). Hence, the sharpness of the viscosity contrast may have a smaller effect on cratonic self-compression compared to the actual magnitude of the lateral viscosity variations. Slow and continuous thickening induced by self-compression may also help to maintain steeper edges for cratonic roots, enhancing their stability.

Geologically, cratons are not individual single units; instead, they are composed of multiple protocratons that together form a larger continental mass (Bleeker, 2003). For example, the North American craton is composed of the Superior, Slave, Wyoming, Hearne, Rae, and several other small blocks (Canil, 2008); the Indian craton is assembled with five smaller units, Dharwar, Bastar, Singhbhum, Bundelkhand, and Aravalli (Pandey, 2020). Since their formation and amalgamation, larger continental units have remained together for more than a couple of billion years. There are some instances of delamination or partial destruction of cratons (Liu et al., 2021; Menzies et al., 1993), but none of them were completely split apart. Self-compression could help to keep smaller continental blocks together within larger cratonic units. It also may be a key reason that older continental units did not split away during supercontinental break-up events. In the future, time-dependent numerical models should be developed to study the effect of self-compression in the craton stabilization process.

6. Conclusions

The diversion of mantle flow by thick and viscous cratonic lithosphere induces self-compression within the cratons themselves. Traction magnitudes increase along the craton periphery, and their directions become convergent toward craton interiors. Traction magnitudes depend on the viscosity structure of the craton, asthenosphere, and lithosphere. In the presence of a 100× viscous craton, traction magnitude increases to 15–20 MPa (Figures 1b–1i), more than an order of magnitude larger than cases without cratons (Figure 1a). The inward-directed orientation of tractions along the craton boundary appears to be a universal phenomenon (Figure 1b, Figure S1 in Supporting Information S1), except for the southernmost part of the African craton (Figure 1h). We infer that such convergent tractions originate from the diversion of (typically downward) mantle flow due to thick and viscous cratonic roots. We test our hypothesis by calculating the ratio of the horizontal gradient of vertical velocity (RHG,

Equation 5). Our calculations demonstrate that large velocity gradients along craton margins amplify tractions along the craton periphery. For most cratons the downward diversion of mantle flow produces inward-directed tractions that induce a compressive stress regime within all cratons. The South African craton presents the only exception, where upwelling flow generates extension. We conclude that self-compression could be a key mechanism that drives the slow and gradual thickening of cratons, enhancing their stability. Such compression may also hold multiple smaller cratons together, merging them into larger blocks. Cratonic self-compression thus may be an essential stabilizing component that allows cratons to resist the destructive forces of mantle convection over billion years.

Data Availability Statement

The latest version of CitcomS code is freely available for download on GitHub (https://github.com/geodynamics/citcoms). Example input files and the model output can be downloaded from JP's personal GitHub repository: https://jyotirmoyp.github.io/research/craton/ or https://doi.org/10.5281/zenodo.7264900. Detailed mathematical calculations and formulations are given in text which can be used to reproduce the results.

Acknowledgments
The finite element code CitcomS code is maintained by Computational Infrastructure for Geodynamics (https://geodynamics.org/). All models were developed in Cray XC40 system at the Supercomputer Education and Research Centre (SERC), IISc. The expenses for the high-priority computational facility was supported by Grant IE/REDA-20-1994 to AG from the Indian Institute of Science–Institution of Eminence (IISc-IOE). JP was partially funded by SERB Grant CRG/2020/004963 from the Department of Science and Technology (DST), Govt. of India. This work was partially supported by the Norwegian Research Council projects 223272 (Centre of Excellence) and 288449 (MAGPIE Project). TWB was partially support by NSF EAR 1925939 and 1853856. JP acknowledges Debanjan Pal for helping with data management and running a few accessory models for this project. Figures were prepared using GMT 6.0.0 and python. The research publication is funded by the Deutsche Forschungsgemeinschaft (DFG, German Research Foundation) - 491138248 and the Open Access Publication Fund of the University of Bayreuth. We thank Graham Pearson and Adam Beall for providing constructive suggestions that helped in improving the quality of the manuscript. Open Access Publishing Fund of the University of Bayreuth.

References

Auer, L., Boschi, L., Becker, T., Nissen-Meyer, T., & Giardini, D. (2014). Savani: A variable resolution whole-mantle model of anisotropic shear velocity variations based on multiple data sets. *Journal of Geophysical Research: Solid Earth*, *119*(4), 3006–3034. https://doi.org/10.1002/2013jb010773

Beall, A., Moresi, L., & Cooper, C. (2018). Formation of cratonic lithosphere during the initiation of plate tectonics. *Geology*, *46*(6), 487–490. https://doi.org/10.1130/g39943.1

Becker, T. W. (2006). On the effect of temperature and strain-rate dependent viscosity on global mantle flow, net rotation, and plate-driving forces. *Geophysical Journal International*, *167*(2), 943–957. https://doi.org/10.1111/j.1365-246x.2006.03172.x

Bedle, H., Cooper, C. M., & Frost, C. D. (2021). Nature versus nurture: Preservation and destruction of Archean cratons. *Tectonics*, *40*(9), e2021TC006714. https://doi.org/10.1029/2021tc006714

Bleeker, W. (2003). The late Archean record: A puzzle in ca. 35 pieces. *Lithos*, *71*(2–4), 99–134. https://doi.org/10.1016/j.lithos.2003.07.003

Canil, D. (2008). Canada's craton: A bottoms-up view. *Geological Society of America Today*, *18*(6), 4–10. https://doi.org/10.1130/gsat01806a.1

Conrad, C. P., & Lithgow-Bertelloni, C. (2006). Influence of continental roots and asthenosphere on plate-mantle coupling. *Geophysical Research Letters*, *33*(5), L05312. https://doi.org/10.1029/2005GL025621

Cooper, C., & Conrad, C. P. (2009). Does the mantle control the maximum thickness of cratons? *Lithosphere*, 1(2), 67–72. https://doi.org/10.1130/l40.1

Cooper, C., Farrington, R., & Miller, M. (2021). On the destructive tendencies of cratons. *Geology*, *49*(2), 195–200. https://doi.org/10.1130/g48111.1

Currie, C. A., & van Wijk, J. (2016). How craton margins are preserved: Insights from geodynamic models. *Journal of Geodynamics*, *100*, 144–158. https://doi.org/10.1016/j.jog.2016.03.015

Gung, Y., Panning, M., & Romanowicz, B. (2003). Global anisotropy and the thickness of continents. *Nature*, *422*(6933), 707–711. https://doi.org/10.1038/nature01559

Jackson, M. G., Konter, J. G., & Becker, T. W. (2017). Primordial helium entrained by the hottest mantle plumes. *Nature*, *542*(7641), 340–343. https://doi.org/10.1038/nature21023

Jordan, T. (1975). The continental tectosphere. *Reviews of Geophysics*, *13*(3), 1–12. https://doi.org/10.1029/rg013i003p00001

Jordan, T. (1978). Composition and development of the continental tectosphere. *Nature*, *274*(5671), 544–548. https://doi.org/10.1038/274544a0

King, S. (2005). Archean cratons and mantle dynamics. *Earth and Planetary Science Letters*, *234*(1), 1–14. https://doi.org/10.1016/j.epsl.2005.03.007

King, S., & Ritsema, J. (2000). African hot spot volcanism: Small-scale convection in the upper mantle beneath cratons. *Science*, *290*(5494), 1137–1140. https://doi.org/10.1126/science.290.5494.1137

Lee, C.-T. A., Luffi, P., & Chin, E. J. (2011). Building and destroying continental mantle. *Annual Review of Earth and Planetary Sciences*, *39*(1), 59–90. https://doi.org/10.1146/annurev-earth-040610-133505

Lenardic, A., & Moresi, L. N. (1999). Some thoughts on the stability of cratonic lithosphere: Effects of buoyancy and viscosity. *Journal of Geophysical Research*, *104*(B6), 12747–12758. https://doi.org/10.1029/1999jb900035

Lenardic, A., Moresi, L. N., & Mühlhaus, H. (2003). Longevity and stability of cratonic lithosphere: Insights from numerical simulations of coupled mantle convection and continental tectonics. *Journal of Geophysical Research*, *108*(B6), 2303. https://doi.org/10.1029/2002JB001859

Liu, J., Pearson, D. G., Wang, L. H., Mather, K. A., Kjarsgaard, B. A., Schaeffer, A. J., et al. (2021). Plume-driven recratonization of deep continental lithospheric mantle. *Nature*, *592*(7856), 732–736. https://doi.org/10.1038/s41586-021-03395-5

Mather, K. A., Pearson, D. G., McKenzie, D., Kjarsgaard, B. A., & Priestley, K. (2011). Constraints on the depth and thermal history of cratonic lithosphere from peridotite xenoliths, xenocrysts and seismology. *Lithos*, *125*(1–2), 729–742. https://doi.org/10.1016/j.lithos.2011.04.003

Menzies, M. A., Fan, W., & Zhang, M. (1993). Palaeozoic and Cenozoic lithoprobes and the loss of >120 km of Archaean lithosphere, Sino-Korean craton, China. *Geological Society, London, Special Publications*, *76*(1), 71–81. https://doi.org/10.1144/gsl.sp.1993.076.01.04

Naliboff, J. B., Conrad, C. P., & Lithgow-Bertelloni, C. (2009). Modification of the lithospheric stress field by lateral variations in plate-mantle coupling. *Geophysical Research Letters*, *36*(22), L22307. https://doi.org/10.1029/2009GL040484

Nataf, H.-C., & Ricard, Y. (1996). 3SMAC: An a priori tomographic model of the upper mantle based on geophysical modeling. *Physics of the Earth and Planetary Interiors*, *95*(1–2), 101–122. https://doi.org/10.1016/0031-9201(95)03105-7

O'Neill, C., Lenardic, A., Griffin, W., & O'Reilly, S. (2008). Dynamics of cratons in an evolving mantle. *Lithos*, *102*(1), 12–24. https://doi.org/10.1016/j.lithos.2007.04.006

Pandey, O. P. (2020). *Geodynamic evolution of the Indian shield: Geophysical aspects*. Springer. https://doi.org/10.1007/978-3-030-40597-7

Paul, J., & Ghosh, A. (2020). Evolution of cratons through the ages: A time-dependent study. *Earth and Planetary Science Letters*, *531*, 115962. https://doi.org/10.1016/j.epsl.2019.115962

Paul, J., Ghosh, A., & Conrad, C. (2019). Traction and strain rate at the base of the lithosphere: An insight into cratonic stability. *Geophysical Journal International*, *217*(2), 1024–1033. https://doi.org/10.1093/gji/ggz079

Pearson, D. G., Scott, J. M., Liu, J., Schaeffer, A., Wang, L. H., van Hunen, J., et al. (2021). Deep continental roots and cratons. *Nature*, *596*(7871), 199–210. https://doi.org/10.1038/s41586-021-03600-5

Polet, J., & Anderson, D. (1995). Depth extent of cratons as inferred from tomographic studies. *Geology*, *23*(3), 205–208. https://doi.org/10.1130/0091-7613(1995)023<0205:deocai>2.3.co;2

Ritsema, J., Deuss, a. A., Van Heijst, H., & Woodhouse, J. (2011). S40RTS: A degree-40 shear-velocity model for the mantle from new Rayleigh wave dispersion, teleseismic traveltime and normal-mode splitting function measurements. *Geophysical Journal International*, *184*(3), 1223–1236. https://doi.org/10.1111/j.1365-246x.2010.04884.x

Rudnick, R., McDonough, W., & O'Connell, R. (1998). Thermal structure, thickness and composition of continental lithosphere. *Chemical Geology*, *145*(3), 395–411. https://doi.org/10.1016/s0009-2541(97)00151-4

Simmons, N. A., Forte, A. M., Boschi, L., & Grand, S. P. (2010). GyPSuM: A joint tomographic model of mantle density and seismic wave speeds. *Journal of Geophysical Research*, *115*(B12), B12310. https://doi.org/10.1029/2010JB007631

Sleep, N. H. (2003). Survival of Archean cratonal lithosphere. *Journal of Geophysical Research*, *108*(B6), 2302. https://doi.org/10.1029/2001JB000169

Wang, H., van Hunen, J., & Pearson, D. G. (2018). Making Archean cratonic roots by lateral compression: A two-stage thickening and stabilization model. *Tectonophysics*, *746*, 562–571. https://doi.org/10.1016/j.tecto.2016.12.001

Wang, H., van Hunen, J., Pearson, D. G., & Allen, M. B. (2014). Craton stability and longevity: The roles of composition-dependent rheology and buoyancy. *Earth and Planetary Science Letters*, *391*, 224–233. https://doi.org/10.1016/j.epsl.2014.01.038

Yoshida, M. (2012). Dynamic role of the rheological contrast between cratonic and oceanic lithospheres in the longevity of cratonic lithosphere: A three-dimensional numerical study. *Tectonophysics*, *532*, 156–166. https://doi.org/10.1016/j.tecto.2012.01.029

Yoshida, M., & Yoshizawa, K. (2021). Continental drift with deep cratonic roots. *Annual Review of Earth and Planetary Sciences*, *49*(1), 117–139. https://doi.org/10.1146/annurev-earth-091620-113028

Zhong, S. (2001). Role of ocean-continent contrast and continental keels on plate motion, net rotation of lithosphere, and the geoid. *Journal of Geophysical Research*, *106*(B1), 703–712. https://doi.org/10.1029/2000jb900364

Zhong, S., Zuber, M., Moresi, L. N., & Gurnis, M. (2000). Role of temperature-dependent viscosity and surface plates in spherical shell models of mantle convection. *Journal of Geophysical Research*, *105*(B5), 11063–11082. https://doi.org/10.1029/2000jb900003